Bitlis Eren University Journal of Science and Technology

Bitlis Eren Üniversitesi Bilim ve Teknoloji Dergisi

Bitlis Eren University Journal of Science and Technology

Bitlis Eren University Journal of Science and Technology

Yıl/Year: 2021 • Cilt/Volume: 11 • Sayı/Issue: 1

Editorial Board

Bitlis Eren University Journal of Science and Technology (Bitlis Eren Univ J Sci & Technol) is an international, refereed open access electronic journal. Research results, reviews and short communications in the fields of Biology (Medicinal, Molecular and Genetics, Veterinary and Agriculture), Physics, Chemistry, Mathematics and Statistics, and also Engineering Sciences are accepted for review and publication. Papers will be published in English. Scientific quality and scientific significance are the primary criteria for publication. Articles with a suitable balance of practice and theory are preferred. Manuscripts previously published in other journals and as book sections will not be accepted.

Bitlis Eren University Journal of Science and Technology indexed in:

- EBSCO

Articles

Influence of deformed potentials on elastic scattering reactions involving deformed projectile-spherical target

Murat AYGÜN [a,*] (iD)

[a] Bitlis Eren University, Department of Physics, TR-13000, Bitlis Turkey

ARTICLE INFO

ABSTRACT

We investigate the effects of potentials with quadrupole and hexadecapole deformations on the elastic scattering angular distributions of deformed projectiles. We calculate the elastic scattering cross-sections of ^{20}Ne + ^{12}C, ^{22}Ne + ^{12}C, ^{24}Mg + ^{24}Mg and ^{28}Si + ^{27}Al reactions by using Deformed Broglia-Winther (1991) (DBW91), Deformed Aage Winther (DAW95) and Deformed Woods-Saxon (DWS) potentials. Then, we perform the calculations for different orientation angles such as θ = 0 and θ = π/2 of deformed projectiles. Finally, we compare the theoretical results together with the experimental data.

1. Introduction

Elastic scattering cross-sections were analyzed extensively for spherical states of nuclei. Different methods including various density distributions [1–3] and nuclear potentials [4–6] were used in order to explain experimental data. However, deformation effect was generally neglected in the calculations. If one or both of nuclei are deformed, the effect of deformation and orientation of nuclei should be included in the analysis of nuclear interactions. In this context, the deformation effect on nuclear reactions was investigated with different studies [7–9]. It is known that the theoretical calculations with deformed case are more difficult. Therefore, different approaches can be found from the literature. One of these is to use a deformed potential. For this purpose, there are different deformed potentials in the literature. As a result, the question of which potential is more valid arises. Thus, we believe that it will be important and useful to investigate the suitability of different deformed potentials for deformed projectiles.

We investigate the effect of deformed potentials on the elastic scattering cross-sections of deformed projectiles. We calculate the elastic scattering cross-sections of ^{20}Ne + ^{12}C, ^{22}Ne + ^{12}C, ^{24}Mg + ^{24}Mg and ^{28}Si + ^{27}Al reactions for three various

deformed potentials such as Deformed Broglia-Winther (1991) (DBW91), Deformed Aage Winther (DAW95) and Deformed Woods-Saxon (DWS). Then, we chose two important orientation angles such as θ = 0 and θ = π/2 where the nucleus can be found. We repeat the theoretical calculations for θ = 0 and θ = π/2 angles of deformed projectiles. We compare our results with the data.

Section 2 gives calculation process. Section 3 provides information about deformed potentials. Section 4 shows the results and discussion. Finally, Section 5 is assigned to the summary and conclusion.

2. Calculation procedure

The total potential for deformed projectile and spherical target can be expressed as

$$U(r) = V_c(r) + V(r) + iW(r) \tag{1}$$

where $V_c(r)$, $V(r)$ and $W(r)$ are the Coulomb, real and imaginary potentials, respectively. V_c(r) potential is [10]

* *Corresponding author.* Tel.: +90 (434) 222 0020; fax: +90 (434) 222 9143
E-mail address: maygun@beu.edu.tr
ORCID : *0000-0002-4276-3511 (M. Aygün)*

$$V_C(r) = \frac{1}{4\pi\varepsilon_0} \frac{Z_P Z_T e^2}{r}, \qquad r \geq R_C$$

$$= \frac{1}{4\pi\varepsilon_0} \frac{Z_P Z_T e^2}{2R_C} \left(3 - \frac{r^2}{R_C^2} \right), \quad r < R_C \qquad (2)$$

$$R_c = 1.25(A_P^{\frac{1}{3}} + A_T^{\frac{1}{3}}).$$

$V(r)$ is calculated using DBW91, DAW95 and DWS potentials which are described below. $W(r)$ is assumed as

$$W(r) = -\frac{W_0}{1 + \exp\left(\frac{r - r_w (A_P^{\frac{1}{3}} + A_T^{\frac{1}{3}})}{a_W} \right)} \qquad (3)$$

where W_0, r_w and a_w are the depth, radius and diffuseness parameters, respectively. The elastic scattering cross-sections are acquire via the code FRESCO [11].

3. Deformed potentials

3.1. Deformed Broglia-Winther 1991 (DBW91) potential

The DBW91 potential can be written in the following form

$$V_N^{DBW91}(r,\theta) = -\frac{V_0(\theta)}{\left[1 + \exp\left(\frac{r - R_0(\theta)}{a} \right) \right]} \text{ MeV,} \qquad (4)$$

Where

$$V_0(\theta) = 16\pi \frac{R_P(\theta) R_T}{R_P(\theta) + R_T} \gamma a, \qquad (5)$$

$$R_0(\theta) = R_P(\theta) + R_T + 0.29 \qquad (6)$$

$$R_i(\theta) = (1.233 A_i^{1/3} - 0.98 A_i^{-1/3})[1 + \beta_{20} Y_{20}(\theta) + \beta_{40} Y_{40}(\theta)] \quad (i = P, T) \qquad (7)$$

P and T subscripts indicate the projectile and target, respectively. The β_2 and β_4 values which are traditionally used to symbolize nuclear deformation show quadrupole and hexadecapole deformation parameters of deformed projectiles respectively, and are given in Table 1 [12].

Table 1. The β_2 and β_4 deformation values of deformed projectiles.

Projectile	β_2	β_4
^{20}Ne	0.364	0.207
^{22}Ne	0.384	0.096
^{24}Mg	0.393	-0.012
^{28}Si	-0.363	0.187

3.2. Deformed Aage Winther (DAW95) potential

The DAW95 potential is similar to the DBW91 potential except for [13]

$$a = \left[\frac{1}{1.17(1 + 0.53(A_P^{-1/3} + A_T^{-1/3}))} \right] \text{ fm,} \qquad (8)$$

and

$$R_0(\theta) = R_P(\theta) + R_T, \qquad (9)$$

With

$$R_P(\theta) = (1.2 A_P^{1/3} - 0.09)[1 + \beta_{20} Y_{20}(\theta) + \beta_{40} Y_{40}(\theta)], \ R_T = 1.2 A_T^{1/3} - 0.09 \qquad (10)$$

3.3. Deformed Woods-Saxon (DWS) potential

The DWS potential is assumed as [14]

$$V_N^{DWS}(r,\theta) = -\frac{V_0}{\left[1 + \exp\left(\frac{r - R(\theta)}{a} \right) \right]} \text{ MeV,} \qquad (11)$$

Where

$$R(\theta) = 1.17 + R_P[1 + \beta_{20} Y_{20}(\theta) + \beta_{40} Y_{40}(\theta)] + R_T \quad (i = P, T) \qquad (12)$$

$$R_{P(T)} = (1 + 0.39 I_{P(T)}) A_{P(T)}^{1/3}, \ I_{P(T)} = \frac{N_{P(T)} - Z_{P(T)}}{A_{P(T)}}, \ a = [0.5 + 0.33(I_P + I_T)] \text{ fm} \qquad (13)$$

$I_{P(T)}$, $Z_{P(T)}$, $N_{P(T)}$ and $A_{P(T)}$ are isospin asymmetry, atomic number, neutron number and mass number of projectile(target), respectively. The potential depth V_0 is evaluated as [15]

$$V_0 = -44.16[1 - 0.40(I_P + I_T)] \frac{A_P^{\frac{1}{3}} A_T^{\frac{1}{3}}}{A_P^{\frac{1}{3}} + A_T^{\frac{1}{3}}} \qquad (14)$$

4. Results and Discussion

A comparative analysis of deformed potentials that can be used to explain the elastic scattering cross-sections between deformed projectile and spherical target nuclei was performed. However, it is also possible to consider target nuclei and Coulomb potential as deformed. Thus, they may give also contributions to the cross-sections. Here we investigated the effect of deformation on the projectile without considering other deformed situations. While studying the deformation effect of the projectiles, we assumed their ground states. With this goal, each potential was achieved by using FORTRAN code which was written by us. Then, the FRESCO cards over the acquiring results were formed. As a result of this, the real part of the optical model potential was obtained. In Fig. 1, we showed the distance-dependent changes of the real potentials of deformed different projectile reactions at $\theta = 0$ and $\theta = \pi/2$ orientations. We observed that the real potentials of DBW91 and DAW95 potentials behaved similarly for ^{20}Ne, ^{22}Ne and ^{24}Mg nuclei except for ^{28}Si. The real potential depths of ^{20}Ne, ^{22}Ne and ^{24}Mg nuclei decrease with increasing orientation angle while the depth of ^{28}Si nucleus increases. It was found that the DWS potential was the deepest for all nuclei and all deformed potentials. The effect of the orientation angle for the DWS potential was observed in the tail part of the potential compared to other potentials. In addition, we noticed that this tailing showed a different situation for the ^{28}Si nucleus.
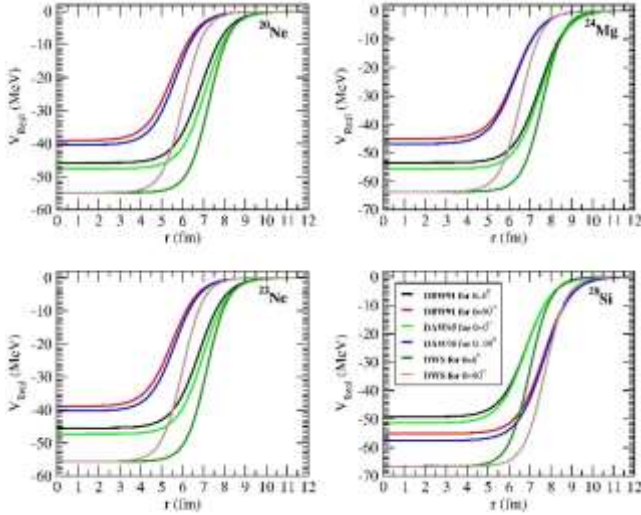
Figure 1. Distance-dependent changes of the real potentials of deformed projectile and spherical target nucleus reactions at different orientations.

The Woods-Saxon potential was applied for the imaginary part of the optical model. The r_w and a_w parameters were investigated in steps of 0.1 fm and 0.01 fm, and the W_0 value was determined for convenient results with the data. Thus, the potential parameters of the reactions were given in Table 2.

Table 2. The W_0 (in MeV), r_w (in fm), a_w (in fm) values used in the calculations of the elastic scattering cross-sections of ^{20}Ne + ^{12}C, ^{22}Ne + ^{12}C, ^{24}Mg + ^{24}Mg and ^{28}Si + ^{27}Al reactions with DBW91, DAW95 and DWS potentials and at $\theta=0$ and $\theta=\frac{\pi}{2}$ orientations.

Reaction	Parameter	DBW91		DAW95		DWS	
		$\theta=0$	$\theta=\frac{\pi}{2}$	$\theta=0$	$\theta=\frac{\pi}{2}$	$\theta=0$	$\theta=\frac{\pi}{2}$
^{20}Ne+^{12}C	W_0	84.0	39.5	95.0	43.0	105.0	48.0
	r_w	1.38	1.38	1.38	1.38	1.38	1.38
	a_w	0.88	0.88	0.88	0.88	0.88	0.88
^{22}Ne+^{12}C	W_0	80.0	39.0	89.0	38.0	93.0	44.0
	r_w	1.38	1.38	1.38	1.38	1.38	1.38
	a_w	0.88	0.88	0.88	0.88	0.88	0.88
^{24}Mg+^{24}Mg	W_0	1.00	1.00	1.00	1.00	1.00	1.00
	r_w	1.38	1.38	1.38	1.38	1.38	1.38
	a_w	0.88	0.88	0.88	0.88	0.88	0.88
^{28}Si+^{27}Al	W_0	1.00	1.10	1.00	1.00	1.00	1.00
	r_w	1.38	1.38	1.38	1.38	1.38	1.38
	a_w	0.88	0.88	0.88	0.88	0.88	0.88

We calculated the elastic scattering cross-sections of ^{20}Ne + ^{12}C reaction at 390 MeV and ^{22}Ne + ^{12}C reaction at 264 MeV by using DBW91, DAW95 and DWS potentials for θ = 0 and θ = $\pi/2$. We compared the theoretical results together with the experimental data for ^{20}Ne + ^{12}C in Fig. 2 and for ^{22}Ne + ^{12}C in Fig. 3. We observed that deformed potentials gave an average behavior in explaining the experimental data that exhibit an oscillating structure. In addition, all the potentials for these reactions were seen to produce a marked phase shift at different orientation angles.
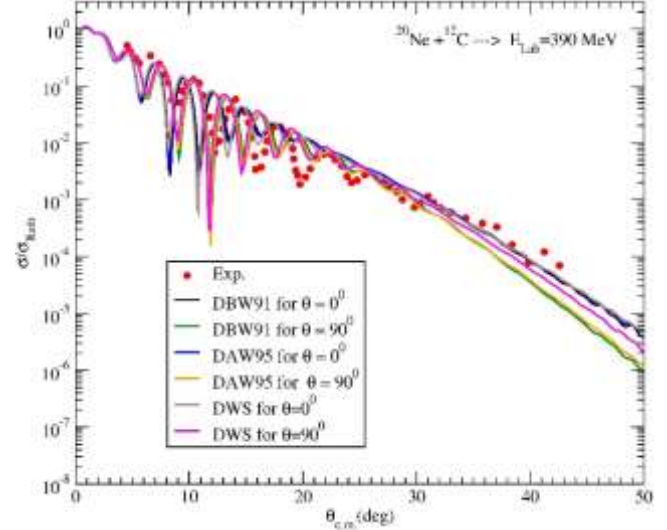
Figure 2. The elastic scattering cross sections of ^{20}Ne + ^{12}C reaction at 390 MeV by using DBW91, DAW95 and DWS potentials for θ = 0 and θ = $\pi/2$. The data are from Ref. [16].
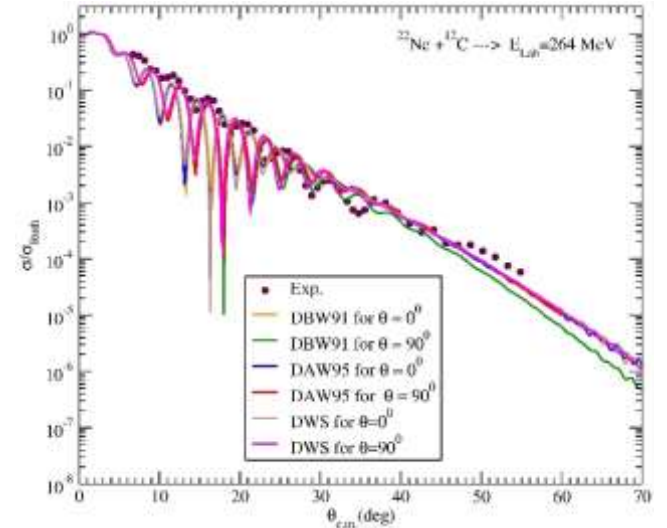
Figure 3. Same as Fig. 2, but for ^{22}Ne + ^{12}C reaction at 264 MeV. The data are from Ref. [17].

Then, we obtained the elastic cross-sections of ^{24}Mg + ^{24}Mg reaction at 60 MeV and ^{28}Si + ^{27}Al reaction at 70 MeV. The calculations were based on DBW91, DAW95 and DWS potentials for θ = 0 and θ = $\pi/2$. We compared the theoretical results with the data for ^{24}Mg + ^{24}Mg in Fig. 4 and for ^{28}Si + ^{27}Al in Fig. 5. The potential results for ^{24}Mg + ^{24}Mg reaction cannot explain the initial values of the experimental data. Although they explain some of the later angles, the results are not in very good agreement with the data in general sense. Additionally, the potentials display a phase shift at different orientation angles. For ^{28}Si + ^{27}Al reaction, it is seen that the results of the deformed potentials are not in good agreement with the experimental data. Especially, for $\theta \geq 47^0$, the potentials are quite inadequate in explaining the experimental data. Also, phase shifts were observed for different orientation angles of the deformed potentials.
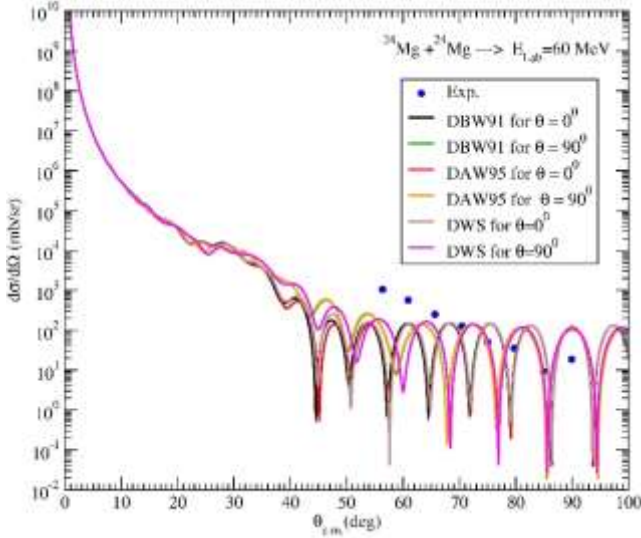
Figure 4. Same as Fig. 2, but for ^{24}Mg + ^{24}Mg reaction at 60 MeV. The data are from Ref. [18].
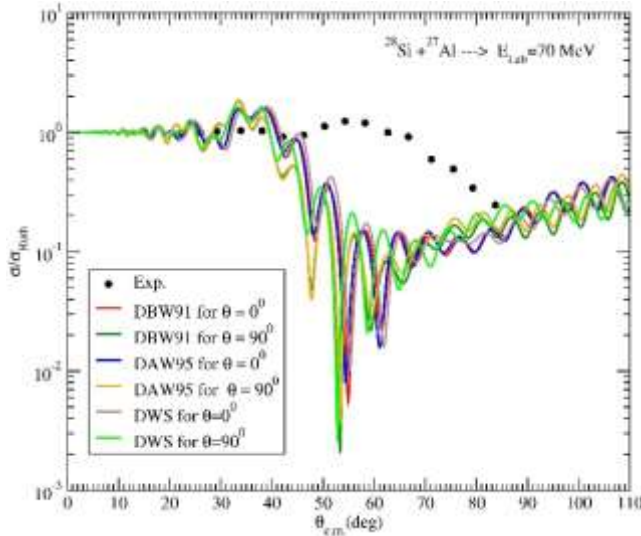
Figure 5. Same as Fig. 2, but for ^{28}Si + ^{27}Al reaction at 70 MeV. The data are from Ref. [18].

One of the remarkable results of our study, all the deformed potentials could not provide good agreement results with the elastic scattering experimental data of ^{24}Mg + ^{24}Mg and ^{28}Si + ^{27}Al reactions although they gave consistent results in defining the elastic scattering experimental data of ^{20}Ne + ^{12}C and ^{22}Ne + ^{12}C reactions. In other words, although the deformed potentials are different from each other, the results were seen to be similar. We think that the structural conditions of the projectiles are more prominent. In this context, we investigated the deformation parameters of all the deformed projectiles. We noticed that the β_2 and β_4 values of ^{20}Ne and ^{22}Ne nuclei are positive, whereas the β_2 and β_4 values of ^{24}Mg and ^{28}Si nuclei are negative. That is, we consider that quadrupole and hexadecapole deformations play a key role in the theoretical calculations.

5. Summary and Conclusions

In our study, the effect of three different deformed potentials such as DBW91, DAW95 and DWS potentials on the analysis of elastic scattering angular distributions of deformed projectile and spherical target was investigated. In this context, although the results of potentials is compatible with the experimental data for ^{20}Ne and ^{22}Ne nuclei, the same results could not be obtained for ^{24}Mg and ^{28}Si nuclei. Especially, the results of ^{28}Si nucleus were seem to be incompatible with data. We concluded that the structural properties of the deformed projectiles were found to be more dominant than the shapes of potentials. Finally, we noticed that the orientation of deformed projectiles affected the shape of the nucleus-nucleus potential well. Therefore, we believe that the deformed potentials used to explain the scattering cross sections of the deformed nuclei should be investigated for further nuclear interactions.

References

[1] Aygun, M., 2018. Analysis with SDHO and RMF density distributions of elastic scattering cross-sections of oxygen isotopes ($^{16-18}$O) by various target nuclei. International Journal of Modern Physics E, 27, 1850055.

[2] Aygun, M., 2019. Analysis with relativistic mean-field density distribution of elastic scattering cross-sections of carbon isotopes ($^{10-14,16}$C) by various target nuclei. Pramana – Journal of Physics, 93, 72.

[3] Aygun, M., Aygun, Z., 2019. Microscopic analysis of elastic scattering cross sections for different densities of ^{8}Li nucleus on light, medium and heavy mass targets. Revista Mexicana de F´ısica, 65, 404-411.

[4] Aygun, M., 2018. Alternative Potentials Analyzing the Scattering Cross Sections of ^{7,9,10,11,12,14}Be Isotopes from a ^{12}C target: Proximity Potentials. Journal of the Korean Physical Society, 73, 1255-1262.

[5] Aygun, M., 2018. The application of some nuclear potentials for quasielastic scattering data of the ^{11}Li + ^{28}Si reaction and its consequences. Turkish Journal of Physics, 42, 302-311.

[6] Aygun, M., 2018. A Comparison of Proximity Potentials in the Analysis of Heavy-Ion Elastic Cross Sections. Ukrainian Journal of Physics, 63, 881-887.

[7] Rashdan, M., Sewailem, Sh. M., 2019. Deformation and orientation effects on reaction cross-sections at intermediate and high energies. International Journal of Modern Physics E, 28, 1950014.

[8] Rashdan, M., 2012. Deformation, orientation, and medium effects in ^{16,19}C + C reactions. Physical Review C 86, 044610.

[9] Hassan, M.Y.M., Farag, M.Y.H., Abul-Magd, A.Y., Nassar, T.E.I., 2008. Nucleus–nucleus reaction cross sections for deformed nuclei. Physica Scripta,78, 045202.

[10] Satchler, G.R., 1983. Direct Nuclear Reactions. Oxford University Press.

[11] Thompson, I. J., 1988. Coupled reaction channels calculations in nuclear physics. Computer Physics Reports, 7, 167.

[12] Möller, P., Sierk, A.J., Ichikawa, T., Sagawac, H., 2016. Nuclear ground-state masses and deformations: FRDM(2012). Atomic Data and Nuclear Data Tables, 109-110, 1-204.

[13] Winther, A., 1995. Dissipation, polarization and fluctuation in grazing heavy-ion collisions and the boundary to the chaotic regime. Nuclear Physics A, 594, 203-245.

[14] Pahlavani, M.R., Alavi, S.A., Tahanipour, N., 2013. Effect of nuclear deformation on the potential barrier and alpha-decay half-lives of superheavy nuclei. Modern Physics Letters A, 28, 16.

[15] Wang, N., Scheid, W., 2008. Quasi-elastic scattering and fusion with a modified Woods-Saxon potential. Physical Review C, 78, 014607.

[16] Bohlen, H.G., Stiliaris, E., Gebauer, B., von Oertzen, W., Wilpert, M., Wilpert, Th., Ostrowski, A., Khoa, D. T., Demyanova, A.S., Ogloblin, A.A., 1993. Refractive scattering and reactions, comparison of two systems: ^{16}O+^{16}O and ^{20}Ne+^{12}C. Zeitschrift fur Physik A, 346, 189-200.

[17] Al-Abdullah, T., Carstoiu, F., Chen, X., Clark, H. L., Fu, C., Gagliardi, C. A., Lui, Y.-W., Mukhamedzhanov, A., Tabacaru, G., Tokimoto, Y., Trache, L., Tribble, R. E., 2010. Physical Review C, 81, 035802.

[18] https://www-nds.iaea.org/exfor/

Physiological and biochemical effects of 2.4-D herbicide in wheat (*Triticum aestivum* L.) varieties

Songül ÇANAKCI GÜLENGÜL[a,*] iD , Fadime KARABULUT[b] iD

[a] Firat University, Department of Biology, TR-23000, Elazıg, Turkey
[b] Firat University, Institute of Science, TR-23000, Elazıg, Turkey

ARTICLE INFO

ABSTRACT

In this work were investigated the physiological and biochemical responses depended on toxic effect caused by different concentrations of herbicides called as 2.4-Dichlorophenoxyacetic acid (2.4-D) herbicide in the seedlings that belong to three wheat varieties. The seeds which belong to wheat (*Triticum aestivum* L. Bayraktar cv., İkizce cv. and Tosunbey cv.) were used as plant material. 15-day old seedlings for each wheat variety were divided into 4 groups consisting of the same number of seedlings and four variety doses of herbicide (0, 100 µM, 300 µM ve 1000 µM) were applied for them. In these applications for seedlings were preferred hydroponic surrounding to root. Although three varieties were increased the growth of root and shoot elongation from the growth parameters of the seedlings, it leaded to a decrease in growth parameters in general in this herbicide. Although 2.4-D in the leaves were caused an increase in 100 µM dose for only the Bayraktar in amount of chlorophyll a+b. In ones except these, there was always been a decreased. The amount of carotenoid was resulted in the reduction of three varieties. Amount of MDA were increased in all three varieties. Glutathione (GSH) / oxidized glutathione (GSSG) ratios in leaves were increased in three varieties. The superoxide dismutase (SOD) activity in the leaves were increased at the Bayraktar and decreased in the İkizce and the Tosunbey. Catalase (CAT) activity showed to a decrease in three varieties. As a result, it was determined that the 2.4-D, which was toxic for wheat plants even in very low concentrations.

1. Introduction

It is known that herbicides can be absorbed by the cultivated plant seeds or weed seeds from soil during germination. However, herbicides move very slowly and hold onto clay and the organic substances in soil and this prevents them from being carried. If herbicides are applied after soil is made fit, their intake by plants increases. Also, a certain amount of herbicide is added in solutions to control the effects of herbicides and prevent them from harming the environment (Güngör 2005). As a result, in damaged plant cells, 2,4-D can bind to protein complexes during photosynthesis, stopping photosynthesis and causing a toxic effect that prevents the maturation of harmful plants (Mander and Liu 2010). Most of the herbicides evaporate from soil and disappear. These are the herbicides included in Thiocarbamate and Phenoxy groups. The herbicides such as 2.4-D, Clomazone, Triallate and Butylate have high vapor pressure. Solar rays cause herbicide molecules to become inactive. This is called chemical degradation. Light is quite important in the degradation of herbicides (Başaran and Serim 2010). Herbicides trigger the formation of the reactive oxygen species which cause oxidative stress. Increased activity of antioxidant enzymes such as SOD and CAT increase is a result of the detoxification mechanism which provides the decrease of lipid peroxidation (Santos and Silva 2015).

* *Corresponding author.*
  E-mail address: *scanakci77@gmail.com*
  ORCID : *0000-0002-5731-6175 (Songül Çanakçı Gülengül)*
  0000-0001-5186-2303 (Fadime Karabulut)

In a study conducted by spraying 23 µM 2.4-D periodically to young and mature leaves of pea plant, oxidative damage in protein and membrane lipids was determined after 72 hours. It was observed that glutathione content increased. Leaves of the mature pea plant had a higher GSH/GSSG rate. In young plant leaves, SOD enzyme activity increased and CAT enzyme activity decreased (Pazmino et al. 2011). 9 macrophyte plants (aquatic) were kept in 2.4-D at concentration of 10-3000 µg/L $^{-1}$. It was observed that the root length of the plant grew more at low concentration and less at high concentration. A decrease was observed in leaf length in the concentration of 300-1000 µg/L $^{-1}$ (Belgers et al. 2007). In a previous study, it was determined that the amount of MDA increased and PRL amount decreased when maize, pea and wheat plants were treated with 2.4-D and atrazine (Alexieva et al. 2003). *Eleusine indica* and *Digitaria adscendens* plants were treated with 100 µM 2.4-D herbicide for 2 days and their root and leaf length decreased and leaf chlorophyll content decreased (Sunohara et al. 2010). In a study examining the effect of atrazine on *Acorus calamus* (sweet edge), *Lythrum salicaria* (Purple loosestrife) and *Scirpus tabernaemontani* (Softstem bulrush) seedlings, it was reported that there was a delay in the plant growth, a decrease in chlorophyll content, and an increase in MDA content (Wang et al. 2015). In a study investigating the effect of imazapic on the leaves of tobacco seedlings, it was reported that catalase activity, carotenoid content, GSH and MDA amounts increased, the plant growth delayed, and the total chlorophyll amounts decreased (Kaya and Doğanlar 2016). Fenoxaprop-p-ethyl herbicide was sprayed to leaves of wheat (*Triticum aestivum* L.) seedlings at the end of 1st, 5th, and 10th days and SOD activity, MDA and GSH amounts increased, CAT activity and chlorophyll amounts decreased and excepted increases and decreases were determined in carotenoids (Akbulut et al. 2018). In the study examining the topic effect on leaves of *Triticum aestivum* L., cv. Mironovskaya 808 (wheat), Secale cereale L. cv. Estafeta tatarstana (rye), and *Zea mays* L. cv. Kollektivnyi 172MV (maize) seedlings, it was reported that the lipid peroxidation, superoxide anion, total antioxidant activity, catalase and ascorbate peroxidase activities increased (Lukatkin et al. 2013).

In this study, the various growth parameters (root-shoot elongation growth, seedling mg dry weight (DW)/g $^{-1}$ fresh weight (FW)) at seedlings of three wheat varieties due to the toxic effect formed by the different concentrations of the 2.4-D herbicide were determined. Pigment analysis, malondialdehyde amount, reduced glutathione/oxidized glutathione rate, superoxide dismutase, and catalase activity were determined in the leaves. It was determined that the 2.4-D herbicide, which was toxic for wheat plants even in very low concentrations. 2,4-D herbicide is effective both in the control of a synthetic auxin hormone derivative and weeds in agricultural areas. Plants cause disorders in many plant functions, such as phloem transport, absorption and photosynthesis, when used or exposed in excess of 2,4-D herbicide. The fact that this herbicide, which is prohibited in Europe, is obtained very easily and with low cost in Turkey and

unconsciously used threatens both our agriculture and health severely.

2. Materials and Methods

2.1. Applications to plant material

In order to grow wheat seedlings which are our experiment material, completely uniform seeds were selected (*Triticum aestivum* L., Bayraktar cv., İkizce cv. and Tosunbey cv.), soaked with tap water and kept in the dark at 23-25°C for 6 hours. At the end of this period, the seeds were placed in germination boxes with lids where they could breathe and left to germinate in the dark at 23-25oC for 3 days. Then germinated seeds with equal length of radicula were selected (homogenous) and planted in pots filled with a mixture of sand (3/1) and field soil (3/2) previously prepared in certain proportions. Seedlings were watered twice a week with an equal amount of tap water in the long day period (16/8) until 15 days in normal daylight. Of these seedlings, completely homogenous growing seedlings were selected and used as experimental material. 15 days of wheat seedlings were divided into 4 groups containing equal number of seedlings and pure water in 250 ml dark glass containers was used as hydroponic medium. Seedlings were exposed to 2.4-D (Alfa aeser) (0, 100 µM, 300 µM, and 1000 µM) at different concentrations for 1 day. All physiological and biochemical analyses were replicated three times for each treatment. For each analysis, 2 g of leaf tissue was used.

2.2. Determination of chlorophyll (a + b) and carotenoid content

0.5 g of fresh leaf tissue was used separately from all treated groups. The leaf tissue, which was cut into small pieces in a sterile mortar, was crushed with 40 ml of 80% acetone for 3-4 minutes and a green extract was obtained. Later, this extract was filtered by vacuuming through a buffer funnel. The remaining residue was crushed again with 30 ml of 80% acetone. This process was continued until the color of the residue completely discolored, and the filtrates were combined by filtration through the buhner funnel. The remaining colorless residue was washed with 80% acetone and the final volume of the total filtrate was completed to 100 ml. All these operations were done separately for each group. Then, the absorbances of the extracts at 440, 645, 652 and 663 nm wavelengths were read against the curve in the spectrophotometer (Shimadzu UVmini-1240). From the absorbance values obtained, mg.g^{-1} pigment was determined in fresh weight (Witham 1971).

2.3. Getting growth parameters

For this purpose, since homogenous seedlings were used initially in all groups, only final height measurements were taken as basis and height differences were calculated. After the 2,4-D herbicide application, the final weights of the seedlings

were determined. Dry weights fixed at intervals of 3-6 hours were determined in 105ºC oven by making suitable packaging and markings. Thus, the amount of dry matter per fresh weight was determined (mg^{-1}DW.G^{-1} FW) (Baltepe et al., 1982).

2.4. Malondialdehyde (MDA), reduced glutathione (GSH) \ oxidized glutathione (GSSG) ratio analysis

2 g of fresh leaves were taken, placed in falt tubes and homogenized for 4 minutes by adding 10 ml Tris (hydroxymethyl) aminomethane (TRIS Base, TRIS HCL, Ethylenediaminetetraacetic acid (EDTA)). The mixtures in falcon tubes were centrifuged (Hettich zentrifugen universal 32 R) at 6000-7000 rpm for 10 minutes. Phase separation occurred at the end of this process. 1 ml glass samples taken from the supernatant (upper phase) of each sample were put into test tubes. 1 ml of 10% perchloric acid (10 ml of perchloric acid, 90 ml of pure water soluble) was added to it and it is waited for two hours at +4°C for 10 minutes at 5000 rpm. centrifuged. Then, 1 ml was taken and measured in HPLC (High performance liquid chromatography, Shimadzu prominence-İ LC-2030C) by taking into vials (Yilmaz et al. 2009, Karataş et al. 2002).

2.5. Superoxide dismutase (SOD; EC 1.15.1.1) analysis

The upper phase was taken to the epondorf. 2.6 ml sod buffer, 100 µl sample, 250 µl epinephrine, 50 µl xanthinoxidase (XO) were added to the glass tubes, respectively. This mixture was vortexed and kept in the dark for 30 minutes. Then, the absorbances of the extracts at 485 nm wavelengths were read against the curve in the spectrophotometer (Mourente et al. 1999).

2.6. Catalase (CAT; EC 1.11.3.6) analysis

The upper phase was taken to the epondorf. 1.9 ml phosphate buffer, 100 µl sample was taken into the glass tubes and absorbance was measured at 240 nm, 1 ml of H2O2 was added and a measurement of up to 60 seconds was made in 15 seconds (Aebi, 1984).

2.7. Statistical analyses

The results were analyzed using one-way ANOVA (SPSS 15.0 Evaluation Version Production Mode Facility). The difference between treatments was considered significant at p<0.01-0.05. Duncan's test was performed to compare means.

3. Results

3.1. Growth parameters

When the effects of the treatments performed on the seedlings on the growth parameters of the roots and leaves were examined, significant differences were determined in all groups.

Decreases of 7.69%, 26.92%, and 50% were determined in the root lengths of the seedlings treated with 2.4-D herbicide in the 100 µM, 300 µM and 1000 µM concentrations of Bayraktar wheat, respectively, compared to the control group. A decrease of 44%, 18.67%, and 9.33% were determined in 100 µM, 300 µM and 1000 µM concentrations, respectively, in İkizce wheat. Decreases of 19.78%, 20.88%, and 15,38% were determined in 100 µM, 300 µM and 1000 µM concentrations in Tosunbey, respectively (P≤0.05) (Table 1).

A decrease of 54.17%, 16.67% and a decrease of 91.67% were determined in the offshoot lengths of the seedlings treated with 2.4-D herbicide in the 100 µM, 300 µM and 1000 µM concentrations, respectively, Bayraktar wheat, compared to the control group. A decrease of 45.71% and increases of 34.29%, and 5.71% were determined in 100 µM, 300 µM and 1000 µM concentrations in İkizce wheat, respectively. Decreases of 90.63%, 3.13%, and 56.25% were detected in 100 µM, 300 µM and 1000 µM concentrations, respectively, in Tosunbey wheat (P≤0.05) (Table 1).

Decreases of 12.19%, 28.08% and 26.89% were determined in the dry weight amounts (mg KA. g^{-1} TA) per fresh weight in the seedlings treated with 2.4-D herbicide in the 100 µM, 300 µM, and 1000 µM concentrations in Bayraktar wheat, respectively, compared to the control group. Decreases of 11.60%, 13.63%, and 33.39% were determined in 100 µM, 300 µM, and 1000 µM concentrations, respectively in İkizce wheat. Decreases of 23.55%, 22.11%, and 48.55% were determined in 100 µM, 300 µM and 1000 µM concentrations, respectively in Tosunbey wheat (P≤0.05) (Table 1).

3.2. Changes in the amounts of chlorophyll (a+b) and carotenoid

Decreases of 7.24%, 9.94%, and 1.67% were determined in the leaves of the 2.4-D-treated seedlings in terms of amount of photosynthetic pigment in 100 µM, 300 µM, and 1000 µM concentrations, respectively, in Bayraktar wheat, compared to the control group. Decreases of 2.35%, 9.52%, and 12.81% were determined in 100 µM, 300 µM, and 1000 µM concentrations, respectively, in İkizce wheat. Decreases of 5.39%, 10.77%, and 13.97% were determined in 100 µM, 300 µM, and 1000 µM concentrations, respectively, in Tosunbey wheat (P≤0.05) (Table 1).

Decreases of 7.98%, 9.20%, and 10.89% were determined in the leaves of the seedlings to which 2.4-D herbicide was treated in terms of carotenoid amounts in 100 µM, 300 µM and 1000 µM concentrations, respectively, in Bayraktar wheat, compared to the control group. Decreases of 2.49%, 3.07%, and 4.02% were determined in 100 µM, 300 µM, and 1000 µM concentrations, respectively, in İkizce wheat. Decreases of 8.01%, 8.54%, and 9.52% were determined in 100 µM, 300 µM,

and 1000 μM concentrations, respectively in Tosunbey wheat (P≤0.05) (Table 1).

Table 1. Root shoot height, dry weight and amounts of photosynthetic pigments changes in the *Triticum aestivum* L. Bayraktar cv., İkizce cv. and Tosunbey cv. seedlings applied to 2.4-D

GROUPS	Seedling Growth (mm/cm^{-1})		Dry Weight (mg DW/g^{-1} FW)	Chlorophyll (a+b) (mg.g^{-1} FW)	Carotenoid (mg.g^{-1} FW)
	ROOT	SHOOT			
B-Control	0,026±0,068	0,024±0,003	0,755±0,042	1.257±0.015	0.652±0.002
B-100 μM	0,024±0,012	0,011±0,014*	0,663±0,050	1.348±0.014*	0.600±0.002*
B-300 μM	0,019±0,021	0,020±0,006*	0,543±0,050*	1.132±0.014*	0.592±0.002*
B-1000 μM	0,013±0,012	0,002±0,007*	0,552±0,060*	1.236±0.014*	0.581±0.002*
İ-Control	0,075±0,017	0,035±0,005	0,638±0,039	1.491±0.015	0.522±0.001
İ-100 μM	0,042±0,012*	0,019±0,009*	0,564±0,040	1.456±0.013	0.509±0.002*
İ-300 μM	0,061±0,009*	0,047±0,013*	0,551±0,021	1.349±0.015*	0.506±0.002*
İ-1000 μM	0,068±0,020*	0,037±0,008*	0,425±0,029*	1.300±0.015*	0.501±0.002*
T-Control	0,091±0,032	0,032±0,007	0,692±0,039	1.467±0.014	0.562±0.002
T-100 μM	0,073±0,012*	0,003±0,003*	0,529±0,036*	1.388±0.018*	0.517±0.002*
T-300 μM	0,072±0,011*	0,031±0,008*	0,539±0,021*	1.309±0.011*	0.514±0.003*
T-1000 μM	0,077±0,007*	0,014±0,007*	0,356±0,032*	1.262±0.014*	0.510±0.003*

*:Compared to the control group at p≤0.05 probability levels. Values are mean of three replicates, Bayraktar: B, İkizce: İ, Tosunbey: T

3.3. Changes in reduced glutathione (GSH)/oxidized glutathione (GSSG) ratios

Increases of 14.78% and 20.39% and a decrease of 33.41% were determined in the GSH/GSSG ratio in the leaves of the seedlings treated with 2.4-D herbicide in the 100 μM, 300 μM, and 1000 μM concentrations, respectively, in Bayraktar wheat compared to the control group. Increases of 5.10% and 24.47% and a decrease of 24.88% were determined in 100 μM, 300 μM and 1000 μM concentrations, respectively, in İkizce wheat. Increases of 36.63%, 113.19%, and 56.47% were determined in 100 μM, 300 μM and 1000 μM concentrations, respectively, in Tosunbey wheat (P≤0,05) (Table 2).

3.4. Changes in malondialdehyde (MDA) amount

Increases of 62.51%, 86.76% and 75.96% were determined in the MDA amounts of the leaves of the seedlings treated with 2.4-D herbicide in the 100 μM, 300 μM, and 1000 μM concentrations, respectively, in Bayraktar wheat, compared to the control group. A decrease of 7.74%, an increase of 16.01%, and a decrease of 18.95% were determined in 100 μM, 300 μM, and 1000 μM concentrations, respectively, in İkizce wheat. Increases of 18.98%, 25.43%, and 62.87% were determined in 100 μM, 300 μM, and 1000 μM concentrations, respectively in Tosunbey wheat (P≤0.05).

3.5. Changes in superoxide dismutase (SOD) activity

Increases of 24.43%, 111.36% and 89.20% were determined in the SOD activity in the leaves of the seedlings treated with 2.4-D herbicide in the 100 μM, 300 μM and 1000 μM concentrations, respectively, for Bayraktar wheat compared to the control group. Decreases of 10.02%, 23.31%, and 5.59% were determined in 100 μM, 300 μM and 1000 μM concentrations in İkizce wheat, respectively. Decreases of 10.26%, 19.33%, and 34.13% were determined in 100 μM, 300 μM and 1000 μM concentrations, respectively, in Tosunbey wheat (P≤0.05) (Table 2).

3.6. Changes in catalase (CAT) activity

Decreases of 49.62%, 42.83% and 5.51% were determined in the CAT activity in the leaves of the seedlings treated with 2.4-D herbicide in the 100 μM, 300 μM and 1000 μM concentrations, respectively, for Bayraktar wheat compared to the control group. Decreases of 50.39%, 27.17%, and 38.55% were determined in 100 μM, 300 μM and 1000 μM concentrations, respectively, in İkizce wheat. Decreases of 44.79%, 54.88%, and 50.65% were determined in 100 μM, 300

μM and 1000 μM concentrations of Tosunbey wheat, respectively (P≤0.05) (Table 2).

Table 2. GSH/GSSG, MDA amounts, SOD and CAT activities changes in the *Triticum aestivum* L. Bayraktar cv., İkizce cv. and Tosunbey cv. seedlings applied to 2.4-D

GROUPS	GSH/GSSG	MDA (nmol.g-1 FW)	SOD unite/gr	CAT (µg/g)
B-Control	10.557±0.272	296.375±17.804	0.176±0.037	339.159±16.336
B-100 µM	12.117±0.318	481.625±20.450*	0.219±0.050	170.874±11.210*
B-300 µM	12.710±1.126*	553.50±59.540*	0.372±0.044*	193.887±4.375*
B-1000 µM	7.030±0.495*	521.510±46.813*	0.333±0.062	320.460±3.135*
İ-Control	6.410±0.860	284.250±1.635	0.429±0.016	309.673±11.303
İ-100 µM	6.737±0.919	262.250±10.687	0.386±0.038	153.614±1.246*
İ-300 µM	8.171±1.180	329.750±14.126	0.329±0.022*	225.531±3.805*
İ-1000 µM	4.815±0.504	230.375±50.326	0.405±0.027	190.291±3.296*
T-Control	8.097±0.696	133.667±16.598	0.419±0.253	356.419±2.491
T-100 µM	11.063±0.949*	159.043±15.510	0.376±0.034	196.764±2.491*
T-300 µM	17.262±1.196*	167.660±8.747	0.338±0.026	160.806±7.610*
T-1000 µM	3.525±0.036*	217.710±5.135*	0.276±0.042*	175.908±2.593*

*:Compared to the control group at p≤0.05 probability levels. Values are mean of three replicates, Bayraktar: B, İkizce: İ, Tosunbey: T

4. Discussion

In the present study, the responses of wheat seedlings to different concentrations of 2.4-D herbicides were investigated. Bayraktar wheat increased in the root lengths of the seedlings treated with 2.4-D herbicide. In İkizce wheat increased in 300 μM and 1000 μM concentrations. At all concentrations of Tosunbey wheat and 100 μM concentration of İkizce decreased. The offshoot lengths of the seedlings treated with 2.4-D herbicide were determined an increase in 300 μM and a decrease in 100 μM and 1000 μM concentrations for Bayraktar wheat. In İkizce wheat were determined a decrease of 100 μM and increases of 300 μM and 1000 μM concentrations. Tosunbey wheat decreased in 100 μM 300 μM and 1000μM concentrations. At all concentrations of 2.4-D herbicide caused a significant decrease in terms of ratio of dry weight per fresh weight in wheat seedlings. It was found that 2.4-D treatment was most inhibitive on the root length among the growth parameters and this effect was the most apparent in Tosunbey wheat (Belgers et al. 2007, Sunohara et al. 2010). It was determined that 2.4-D (Belgers et al. 2007; Sunohara et al., 2010) application caused very effective growth delays on the offshoot lengths of wheat seedlings, especially in Tosunbey wheat. 2.4-D (Santos and Silva 2015) herbicide caused a significant decrease in terms of the dry weight amounts of wheat seedlings, especially in Tosunbey wheat.

Chlorophyll (a+b) contents in leaves of wheat seedlings decreased in all concentrations of 2.4-D herbicide. Carotenoid contents in leaves of wheat seedlings were influenced by 2.4-D herbicide in other words pigment breakdown increased (Santos and Silva 2015). The chlorophyll content of plants changes under stress. The reason for the decrease in chlorophyll content is the oxidative stress induced by herbicides. Because chlorophyllase enzyme and chlorophyll degradation increase under stress conditions (Kaya and Doğanlar 2016). The herbicide treatment causes important photo-dynamic damages in the photo-system by photo-inhibition and decreases photosynthesis production. Herbicides cause oxidative stress in chloroplasts and lead to the increase of the reactive oxygen species and, therefore, lead to the damage of the photosynthetic devices due to chlorophyll degradation (Santos and Silva 2015). In terms of chlorophyll (a+b) amounts, 2.4-D herbicide caused significant decreases mostly in Tosunbey wheat (Sunohara et al. 2010, Wang et al. 2015, Kaya and Doğanlar 2016). In terms of carotenoid amounts in wheat seedlings; the pigment destruction increased mostly in Bayraktar wheat (Santos and Silva 2015) in 2.4-D treatment. In macroscopic terms, necrosis and chlorosis were observed intensely in the leaves of the seedlings treated with the aforementioned herbicides and softening was reported, especially in roots, due to tissue destruction. Carotenoids play a shield-protection mechanism role against oxidative damage. Carotenoids included in chloroplast protect chlorophyll against free radicals in photo-oxidation risk and

they do this by reacting with free radicals themselves. Chlorophyll molecules which are stimulated by taking photon react with oxygen, singlet oxygen shape, superoxide anion, hydroxyl radicals, and hydrogen peroxide. This harms especially lipid derivative compounds included in cells and membrane systems. Thus, these pigments are exposed to oxidative damage due to stress (Santos and Silva 2015).

In the MDA amounts increased in the leaves of the Bayraktar wheat seedlings treated with 2.4-D herbicide (Alexieva et al. 2003, Wang et al. 2015, Kaya and Doğanlar 2016, Lukatkin et al. 2013). While MDA amounts in leaves of wheat seedlings caused an increase only 300 µM concentration, regarding 100 µM and 1000 µM concentrations determined a decrease in leaves of İkizce wheat. MDA amounts in leaves of Tosunbey wheat seedlings also increased in 100 µM, 300 µM, and 1000 µM concentrations. 2.4-D herbicide had an increasing effect mostly in Bayraktar wheat in the leaves of Bayraktar wheat seedlings in terms MDA amount (Alexieva et al. 2003, Wang et al. 2015, Kaya and Doğanlar 2016, Lukatkin et al. 2013). Akbulut and Yiğit (2010) reported in their study conducted on maize (*Zea mays* cv. Martha F1) seedlings that Atrazine herbicide caused an increase in MDA amount when it was treated at low dose and it caused a decrease in MDA amount when it was treated at high dose. Significant increases have been determined in the groups included in the studies in MDA amount, which is another important parameter demonstrating the oxidative stress intensity and is the typical end product of the lipid peroxidation reaction in the cell membrane. Also, it was determined that MDA amount decreased especially for the high herbicide doses (Akbulut and Yiğit 2010). The fatty acid profile (saturated and unsaturated fatty acid rates) in bio-membranes change under oxidative stress. The increase in MDA level showed that the oxidative stress-related lipid peroxidation increased in biomembranes of plants (Wang et al. 2015).

GSH/GSSG ratio of the seedlings treated with 2.4-D herbicide were determined an decrease in 1000 µM and a increase in 100 µM and 300 µM concentrations for Bayraktar and İkizce wheat (Pazmino et al. 2011, Kaya and Doğanlar 2016). The GSH/GSSG ratio of the Tosunbey wheat seedlings treated with 2.4-D herbicide increased in all concentrations (Pazmino et al. 2011, Kaya and Doğanlar 2016). The highest increase was observed in Tosunbey wheat for 2.4-D herbicide in terms of GSH/GSSG ratios in the leaves of wheat seedlings (Pazmino et al. 2011, Kaya and Doğanlar 2016) and a decrease was determined in 1000 µM concentration. Glutathione reductase enzyme (GR) converts oxidized glutathione (GSSG) to reduced glutathione (GSH) with a reaction based on NADPH+. Reduced glutathione is an important antioxidant that plays a role in the defense against oxidative stress and is not enzymatic. The increase in glutathione reductase activity is the indicator of the plant defense in oxidative stress. GSH and GR constitute the compounds of ascorbate-glutathione metabolism which plays a role in reacting to stress in plants (Kaya and Doğanlar 2016; Abou-Zeid et al., 2020).

An increase was determined in Bayraktar wheat in 2.4-D herbicide in the leaves of wheat seedlings in terms of SOD enzyme activity (Pazmino et al. 2011, Santos and Silva 2015) and a decrease was observed in İkizce and Tosunbey wheats (Romero-Puertas et al. 2004). The antioxidant system has an important role in protecting cell components from the damages of reactive oxygen species produced under stress. The production of reactive oxygen species in plant cells is low under optimal growth conditions. However, the increase in the production and accumulation of reactive oxygen species in most of the environmental stresses bring the deterioration of cell homeostasis (Wang et al. 2015). The SOD activity increasing under stress conditions has demonstrated that especially the superoxide radical reactive oxygen species are overproduced. Because it has a role in removing superoxide radical from SOD chloroplasts and superoxide radical is converted to H2O2. Herbicide toxicity is formed when SOD activation, which increases significantly in the antioxidant system, gets involved (Santos and Silva 2015; Sharma et al., 2012; Abou-Zeid et al., 2020; Linu and Girija 2020).

Decreases of CAT activity were determined in the leaves of all the wheat seedlings treated with 2.4-D herbicide in the all concentrations. In terms of CAT enzyme activity in wheat seedling leaves, Tosunbey wheat has the highest decrease in 2.4-D (Pazmino et al. 2011) herbicide (Akbulut et al. 2018). Catalase is found in the organelles named peroxidase in all the plant cells and it keeps H2O2 (H2O+½ O2) level at a certain level for cells and plays a protective role. The catalase enzyme detoxifies H2O2 at high concentration and provides that plant eliminates stress with the least loss. That the activity of antioxidant enzymes such as SOD and CAT increased is a result of the detoxification mechanism which provides a decrease of lipid peroxidation. The oxidative damage in the seedling leaves increases SOD and decreases the other enzymes, thus causing an imbalance in the enzyme activities and probably is associated with the H_2O_2 increase in the chloroplasts (Santos and Silva 2015; Sharma et al., 2012; Abou-Zeid et al., 2020; Linu and Girija 2020).

Consequently, it was determined that the 2.4-D herbicide, which was toxic for wheat plants even in very low concentrations. 2,4-D herbicide is effective both in the control of a synthetic auxin hormone derivative and weeds in agricultural areas. Plants cause disorders in many plant functions, such as phloem transport, absorption and photosynthesis, when used or exposed in excess of 2,4-D herbicide. The fact that this herbicide, which is prohibited in Europe, is obtained very easily and with low cost in Turkey and unconsciously used threatens both our agriculture and health severely. As our results revealing this situation are very limited and, we could not discuss our results in a very large platform and sometimes we had to give the indirect studies as references.

Acknowledgements

References

Abou-Zeid, H., Abdel-Latif, S. A., & Ismail, G. S., 2020. Effect of 2, 4-Dichlorophenoxy Acetic Acid on Antioxidant Systems in a Non-Target Plant (*Zea mays* L.). Catrina: The International Journal of Environmental Sciences, 22(1), 19-27.

Aebi, H., 1984. Catalase in Vitro, Method Enzym. 105: 121-126.

Akbulut, G. B., and Yiğit, E., 2010. The changes in some biochemical parameters in *Zea mays* cv. "Martha F1" treated with atrazine. Ecotoxicology and Environmental Safety 73: 1429-1432.

Akbulut, G. B., Yiğit, E., Kayac, A., and Aktas, A., 2018. Effects of salicylic acid and organic selenium on wheat (*Triticum aestivum* L.) exposed to fenoxaprop-p-ethyl. Ecotoxicology and Environmental Safety 148: 901–909.

Alexieva, V., Ivanov, S., Sergiev, I., and Karanov, E., 2003. Interaction Between Stresses. Bulg. J. Plant Physiol. Special Issue 1-7.

Baltepe, Ş., Bilaloğlu, R. and Yürekli, A. K., 1982. Plant Physiology I (Plant Metabolism) Laboratory Guide, E. Ü. Science Faculty Publications, October, 29, 44-45.

Başaran, M. S., and Serim, A. T., 2010. Degradation of Herbicides by Soil. Selçuk University. Selçuk Journal of Agriculture and Food Sciences 24 (2): 54-61.

Belgers, J. D. M., Lieverloo, R. J. V., Pas, L. J. T. V., and Brink, P. J. V. D., 2007. Effects of the herbicide 2,4-D on the growth of nine aquatic macrophytes. Aquatic Botany 86: 260-268.

Güngör, M., 2005. Investigating the Importance of Chemical Weeding in Maize Cultivation Areas in the City of Adana and The Emerging Problems, postgraduate thesis, Çukurova University, Institute of Science, Adana.

Karataş, F., Karatepe, M., and Baysar, A., 2002. Determination of free malondialdehyde in human serum by high performance liquid chromatography. Anal Biochemistry 311: 76-79.

Kaya, A., and Doğanlar, Z. B., 2016. Exogenous jasmonic acid induces stress tolerance in tobacco (*Nicotiana tabacum*) exposed to imazapic. Ecotoxicology and Enviromental Safety 124: 470-479.

Linu, C., and Girija, T., 2020. Physiological response of rice to herbicide application. Indian Journal of Weed Science, 52(3), 270-275.

Lukatkin, A. S., Gar'kova, A. N., Bochkarjova, A. S., Nushtaeva, O. V., and Silva, J. A. T., 2013. Treatment with the herbicide TOPIK induces oxidative stress in cereal leaves. Pesticide Biochemistry and Physiology, 105: 44-49.

Mander, L., and Liu, HW., 2010. Comprehensive Natural Products II Chemistry and Biology. Elsevier Oxford 3: 205–236.

Mourente, G., Tocher, D. R., Diaz, E., Grau, A., and Pastor, E., 1999. Relationships between antioxidants, antioxidant enzyme activities and lipid peroxidation products during early development in Dentex dentex eggs and larvae. Aquaculture, 179: 309–324.

Pazmıño, D. M., Rodriguez-Serrano, M., Romero-Puertas, M. C., Archilla-Ruız, A., Del Rio, L. A., and Sandalıo, L. M., 2011. Differential response of young and adult leaves to herbicide 2,4-dichlorophenoxyacetic acid in pea plants: role of reactive oxygen species. Plant Cell and Environment, 34: 1874-1889.

Romero-Puertas, M. C., Mccarthy, I., Gomez, M., Sandalıo, L. M., Corpas, F. J., Del Rio, L. A., and Palma, J. M., 2004. Reactive oxygen species-mediated enzymatic systems involved in the oxidative action of 2,4-dichlorophenoxyacetic acid. Plant,Cell and Environment, 27: 1135-1148.

Santos, C. M., and Silva, M. A., 2015. Physiological and biochemical responses of sugarcane to oxidative stress induced by water deficit and paraquat. Acta Physiol. Plant 37: 172.

Sharma, P., Jha, A. B., Dubey, R. S., & Pessarakli, M., 2012. Reactive oxygen species, oxidative damage, and antioxidative defense mechanism in plants under stressful conditions. Journal of botany, 2012.

Sunohara, Y., Shirai, S., Wongkantrakorn, N., and Matsumoto, H., 2010. Sensitivity and physiological responses of Eleusine indica and Digitaria adscendes to herbicide quinclorac and 2,4-D. Environmental and Experimental Botany, 68: 157-164.

Wang, Q., Que, X., Zheng, R., Pang, Z., Li, C., and Xiao, B., 2015. Phytotoxicity assessment of atrazine on growth and physiology of three emergent plants. Environ Sci Pollut Res, 22: 9646-9657.

Witham, F. H., Blaydes, D. F., and Dewlin, R. M., 1971. Experiments in Plant Physiology New york, Von Nonstrand Reinhold Company, 55-56.

Yilmaz, O., Keser, S., Tuzcu, M., Guvenc, M., Cetintas, B., Irtegun, S., Tastan, H., and Sahin, K., 2009. A Practical HPLC Method to Measure Reduced (GSH) and Oxidized (GSSG) Glutathione Concentrations in Animal Tissues. Journal of Animal and Veterinary Advances, 8(2) 343-347.

Geyikli (Çanakkale, Turkey) Heavy Mineral Sands: Insights to Their Origin Related with Alkaline Intrusive Rocks

Ali Tugcan UNLUER[a] [iD], Huseyin KOCATURK[a, *] [iD], Zeynep DONER[a] [iD], Mustafa KAYA[a] [iD]
Demet Kiran YILDIRIM[a] [iD], Mustafa KUMRAL[a] [iD] Senel OZDAMAR[a] [iD]

[a] Istanbul Technical University, Faculty of Mines, Department of Geological Engineering, TR-34467, Istanbul Turkey

A R T I C L E I N F O

A B S T R A C T

Essexites of Kestanbol pluton have significant amount of iron (Fe), titanium (Ti), Rare Earth Elements (REE) and thorium (Th) and considered as the source of Geyikli Heavy Mineral Sands (HMS). Geyikli HMS were enriched by the minerals of magnetite, rutile, monazite and apatite. In Geyikli HMS, REE contents (up to 0,25%) were rised by 4-5 times during placer deposition, mainly caused by the enriching of weathering resistant REE bearing dense phosphate minerals and zircon. On the other hand, Fe (up to 11%) and Ti (up to 2,5%) enrichments are heavily dependent on the magnetite, titanomagnetite and rutile minerals. By using the basic physical mineral processing techniques such sieving, shaking tables, multi gravity seperators, magnetic seperation, it is possible to reach higher grades for both REE and Fe-Ti and to have better initial values for electrochemical mineral processing techniques.

1. Introduction

Heavy Mineral Sand deposits are hosted for a variety of strategic element enrichments which include Rare Earth Elements, Thorium, Uranium, Iron, Titanium and Zircon. In Turkey a few number of heavy mineral placers (Ormanlı, İstanbul; Karasu and Melen Sakarya; Ünye, Ordu;) are identified (Mugan and Ipekoğlu 1995). Most of these mineralizations are relatively small and commercial mining in these placers are not financialy feasible.

The Geyikli Heavy Mineral Sands located in Çanakkale area is one of the most famous placers in Turkey (Andac 1973) This study focuses on the geochemical mineralogical properties of

Geyikli Heavy Mineral Sands and their origin. Previous studies indicated that the main minerals in Geyikli placer are magnetite, sphene, zircon, anatase, korund, thorite and uranothorite (Mücke and Andac, 1975; Örgün et al. 2007). Similar to the other beach sand deposits which originated from felsic or alkaline magmatic rocks, Geyikli placer's main heavy mineral source is Kestanbol pluton (Andac 1973).

2. Material and Methods

Thirteen placer and five essexite samples gathered from the study area during field work. Whole-rock (major and trace element) analyses were conducted on powders grounded using an agate mortar muller milling device. Using a Bruker S8

* *Corresponding author.* Tel.: +90 212 285 6307
  E-mail address: kocaturkhu@itu.edu.tr
  ORCID : 0000-0003-0382-4059 (Ali Tugcan.Unluer), 0000-0002-5131-8807 (Huseyin.Kocaturk), 0000-0003-2928-3174 (Zeynep.Doner), 0000-0003-0694-9754 (Mustafa.Kaya), 0000-0001-5995-5723 (Demet.Yildirim), 0000-0001-7827-8721 (Mustafa.Kumral), 0000-0002-4706-8585 (Senel,Ozdamar)

Tiger X-ray fluorescence (XRF) spectrometer with wavelength ranges from 0.01–12 nm, the oxides of major elements, including SiO_2, Al_2O_3, CaO, K_2O, Na_2O, Fe_2O_3, MnO, MgO, TiO_2, and P_2O_5, were determined; the analytical uncertainty is usually <5%. Elemental analyses were conducted on powders grounded using an agate mortar muller milling device for Elan DRC-e Perkin Elmer Inductively Coupled Plasma-Mass Spectrometry(ICP-MS) in Geochemistry Research Laboratories of Istanbul Technical University (ITU/JAL) to determine the U, Th and REE element contents. A two-step digestion process used approximately 50 mg of powdered samples: (1) 6 ml of 37% HCl, 2 ml of 65% HNO_3 and 1 ml of 38–40% HF acid mixer put in a pressure- and temperature-controlled Teflon beaker using a Berghoff Microwave at 135 °C; (2) 6 ml of 5% boric acid solution was added to the step one mixer for ICP-MS analyses.

3. Geological Setting

Biga Peninsula Northwestern Anatolia (Turkey) widespread Cenozoic magmatism occured in Middle Eocene after the continental collision between the Sakarya Zone and Anatolide–Tauride blocks. As a result of this magmatism, various granitoids were emplaced into the crystalline basement rocks of the Sakarya continent in Eocene-Miocene period with similar geochemical and mineralogical signatures (High-K, calcalkaline, I-type granitoids). N-S trending Kestanbol pluton is an elliptical granitoid body which emplaced into regionally metamorphosed basement rocks. East and southeast borders of the plutonic body is surrounded with Miocene acidic to intermediate volcanic and pyroclastic rocks (rhyolite, rhyodacite lavas and andesitic-trachyandesitic pyroclastic rocks) (Karacık and Yılmaz, 1998). The Plio-Quaternary sedimentary units are observable in west and northwest borders of the pluton (Karacık and Yılmaz, 1998) (Figure 1).
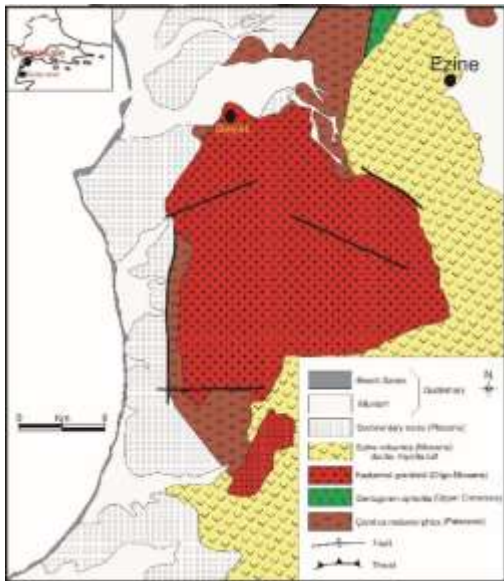

Figure 1. Geological map of the study area modified from Örgün et al., (2007).

4. Petrographical, Mineralogical and Geochemical Properties of Kestanbol Pluton & Geyikli Heavy Mineral Sands

4.1. Petrography of Kestanbol Pluton and Essexites

The pluton is mainly composed of quartzmonzonitic and monzodioritic rocks with a mineral paragenesis of orthoclase, plagioclase, quartz, hornblende, biotite and accessorry minerals magnetite, ilmenite, rutile, pyrite, zircon, allanite, apatite, epidote, thorite and uranothorite (Örgün et al., 2007). In this study it is concluded that the main heavy mineral source rocks are essexitic rocks of the outward zones of Kestanbol pluton, located between Kemallı and Aladağ villages.

The essexites in the study area are described as medium to coarse grained, greyish to greenish colored rocks. These rocks display holocrystalline, hipidiomorphic granular texture or porphyritic in contact zone.

The rocks show evidence for cataclasm and alteration in some zones and made up of pyroxene (30-35% by volume), plagioclase (20-25% by volume), amphibole (20-25% by volume), K-feldpars (20-30% by volume) as major minerals and zircon, apatite, monazite as accesorry minerals (Figure 2).
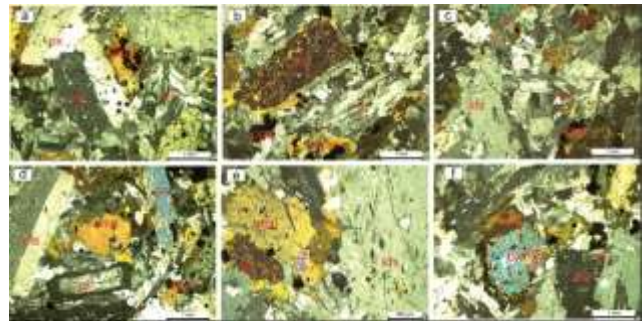

Figure 2. Photomicrographs showing petrographical characteristics of the studied plutonic rock K-feldspars display poiklitic texture (a,c,f); pyroxenes are altered to amphiboles (a,f) plagioclase minerals are shows twining and displays zoned texture.

In pyroxene minerals uralitization and chloritization alterations are common and plagioclase minerals are altered to smectite and secondary calcite minerals. According to the mineralogical data obtained from the rocks can be described as essexite and petrographical studies are consistent with whole rock chemical composition (Table 1).

4.2. Geochemical Studies

Kestanbol granitoid in the region can be considered as alkaline intermediate granitoids. The major-element oxides (in %) and trace & rare earth (REE) elements of Kestenbol monzodiorite (Altunkaynak et al. 2012), essexite and Geyikli HMS are shown in Table 1.

Table 1. Average contents of major-element oxides (in %) and trace & rare earth (REE) elements (in ppm) of the studied Kestenbol essexite and Geyikli Heavy Mineral Sand, with the average content of the Kestanbol monzodiorite from Altunkaynak et al. (2012).

					Major-Element Oxides						
Sample	SiO_2	Al_2O_3	Fe_2O_3	MgO	CaO	Na_2O	K_2O	TiO_2	P_2O_5	MnO	LOI
Kestanbol monzodiorite	60.3	17.4	4.29	1.50	3.77	3.20	6.35	0.45	0.30	0.10	0.52
Kestanbol Essexite	54.1	16.3	6.63	2.52	6.58	3.48	7.17	0.84	0.69	0.13	0.91
Geyikli HMS	52.1	9.32	13.9	1.55	6.16	3.37	4.27	3.17	0.60	0.07	1.12

								Rare Earth and Trace Elements											
Sample	La	Ce	Pr	Nd	Sm	Eu	Gd	Tb	Dy	Ho	Er	Tm	Yb	Lu	∑REE	Y	Th	U	Nb	Zr
Kestanbol monzodiorite	81.0	156.1	15.2	61.4	10.3	3.30	7.58	1.32	4.34	0.76	2.51	0.27	1.76	0.25	346.1	24.5	35.0	7.90	14.6	319
Kestanbol Essexite	121.1	234.2	25.8	95.1	15.7	4.02	12.4	1.70	6.78	1.05	3.18	0.34	2.58	0.38	524.2	31.5	101.6	35.2	70.0	700.0
Geyikli HMS	515.3	1007	109.6	384.0	64.3	8.67	52.8	6.71	32.1	5.36	16.2	1.96	13.4	1.87	2219	155.7	162.0	61.0	153.0	3771

The higher total alkali content in essexites than Kestanbol monzodiorites indicates that the essexitic rocks were formed from a less fractioned magma. The studied essexite samples fall in the A-type and Within-Plate granites sections of geotectonic discrimination diagrams, showing that a strong post-collisional character and slight affinity for Syn-collision granites (Figure 3).
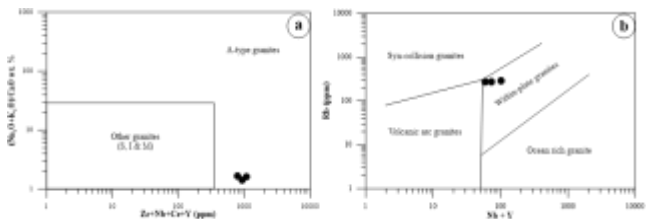

Figure 3. Plots of a) Zr+Rb+Ce+Y vs. (Na_2O+K_2O)/CaO, (Whalen et al, 1987) b) Rb vs. Nb+Y, showing geotectonic discrimination of the studied rocks (Pearce et al. 1984).

Kestanbol granitoid's essexitic rocks are more enriched in terms of the incompatible elements than rocks located in the remaining parts of the granitoid body. This enrichment can be explained with the decreasing of silica and increasing of total alkali content. Studied essexitic rocks show enrichments in both LILE (K, Ba, Sr) and HFSE (REE, Th, U) due to the less fractionated magma and potassic-alkaline nature of the rocks as shown in Figure 4, all Kestanbol rocks show Nb, Ti and P depletion. In addition, the high Pb values indicate the crustal contamination in magma chamber.
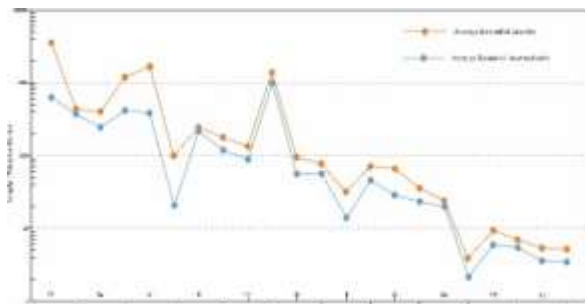

Figure 4. Spider diagram for Essexitic rocks and the remaining average Kestanbol pluton (Sun and Mcdonough 1989).

4.3. Evaluation of the Geyikli Heavy Mineral Sands

The Geyikli HMS are enriched in most of the heavy minerals and related elements such as Fe, Ti, Zr and REE. The Zr and REE contents were enriched 4 to 5 times during placer deposition. Moreover, Heavy Rare Earth Elements (HREE) were more enriched than Light Rare Earth Elements (LREE). It can be stated that the HREE enrichments are closely related with the zircon mineral, having the similar enrichment factors (Figure 5). The positive correlation between P_2O_5 and LREE are observed, pointing out that main LREE bearing minerals are either monazite, xenotime or apatite.

The REE bearing phosphate minerals such as apatite, monazite or xenotime mainly occur in early stages of the fractional crystallization (Kogarko 2018) suggesting that the REE enrichment was not related with any hydrothermal activity in resource rocks.

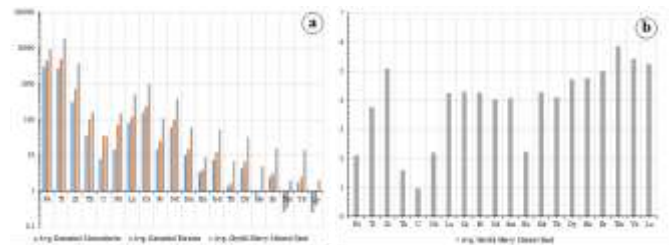**Figure 5.** a) Relative enrichment of elements b) Enrichment factor of Geyikli Heavy Mineral Sand relative to Kestanbol essexite.

Geyikli Heavy Mineral Sands were enriched in heavy minerals such as magnetite, titanomagnetite, hematite zircon, rutile, and apatite according to XRD (Figure 6).
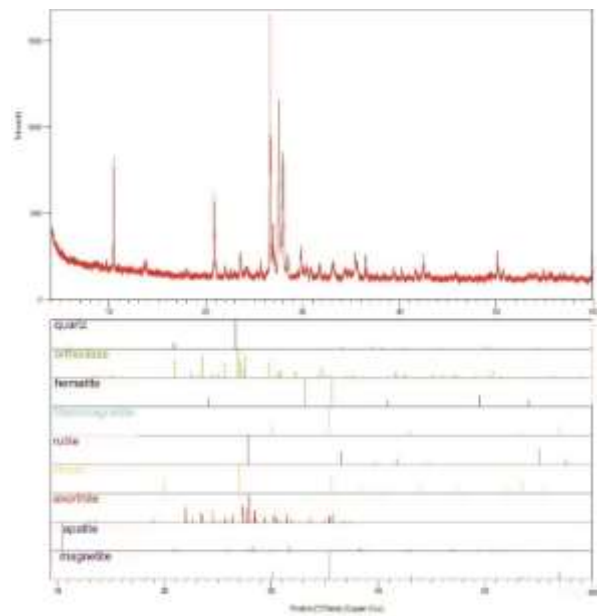

Figure 6. X-Ray diffractogram of Geyikli Heavy Mineral Sand, showing the the mineral composition.

5. Conclusions

The studied rocks were described as essexites by the petrographical analysis. These essexites are located in the borders of Kestanbol pluton have significant amount of incompatible elements and can be considered as a source for REE and Th. It is concluded that these enriched elements within the Geyikli sand are related with REE bearing phosphate minerals. In Geyikli HMS, LREE contents were enriched by 4 times during placer deposition. HREE values, which are closely related with zircon minerals, were more enriched than LREE (up to 5 times). In addition to Geyikli HMS, various nearby locations such as fluvial placers or in-stu enrichments on upper parts of the granitoid body can be considered as depositions of these weathering resistant and dense REE-phosphate minerals.

The Geyikli HMS were enriched by the elements of Fe, Ti and REE-Th. Iron and titanium enrichments largely dependent on the magnetite, titanomagnetite and rutile minerals. For the large scale production, it will be wise to use the basic physical mineral processing techniques (sieving, shaking tables, multi gravity seperators, magnetic separation) to reach higher grades. These higher grade values can easily be used as a better take off point for more complex electrochemical mineral processing (flotation and solvent extraction) techniques.

References

Altunkaynak, Ş., Dilek, Y., Genç, C. Ş., Sunal, G., Gertisser, R., Furnes, H., and Yang, J., 2012. Spatial, temporal and geochemical evolution of Oligo–Miocene granitoid magmatism in western Anatolia, Turkey. Gondwana Research, 21(4), 961-986.

Andaç, M., Biga Yarimadasinda Ezine Siyenit Masifi ile Civarindaki Kayaçlarin Petrografisi Ve Bu Kayaçlardan Meydana Gelen Radyoaktif Sahil Plaser Maden Yataginin Etüdü, 1973 Doçentlik tezi (Istanbul, Turkey 97s: Istanbul Technical University).

Karacık, Z., and Yılmaz, Y., 1998. Geology of the ignimbrites and the associated volcano–plutonic complex of the Ezine area, northwestern Anatolia. Journal of Volcanology and Geothermal Research, 85(1-4), 251-264.

Kogarko, L., 2018. Chemical composition and petrogenetic implications of apatite in the Khibiny apatite-nepheline deposits (Kola Peninsula). Minerals, 8(11), 532.

Mugan, P. A., and İpekoğlu, B., 1995. Akçakoca-Kefken (KB Türkiye) arasında yer alan sahil kumlarının ağır mineral içerikleri. Bilimsel Madencilik Dergisi, 34(2), 27-38.

Mücke, A., and Andaç, M., 1975. Die Paragenese der Schwermineralseifen Südlich von Troja (Westtürkei). Maden Tetkik ve Arama Dergisi, 85(85).

Örgün, Y., Altınsoy, N., Şahin, S. Y., Güngör, Y., Gültekin, A. H., Karahan, G., and Karacık, Z., 2007. Natural and anthropogenic radionuclides in rocks and beach sands from Ezine region (Çanakkale), Western Anatolia, Turkey. Applied Radiation and Isotopes, 65(6), 739-747.

Pearce, J. A., Harris, N. B., and Tindle, A. G., 1984. Trace element discrimination diagrams for the tectonic interpretation of granitic rocks. Journal of petrology, 25(4), 956-983.

Sun, S. S., and McDonough, W. F., 1989. Chemical and isotopic systematics of oceanic basalts: implications for mantle composition and processes. Geological Society, London, Special Publications, 42(1), 313-345.

Whalen, J. B., Currie, K. L., and Chappell, B. W., 1987. A-type granites: geochemical characteristics, discrimination and petrogenesis. Contributions to mineralogy and petrology, 95(4), 407-419.

Spectroscopic characterization and structural insights of 4-Coumarinyl-4-nitrobenzoate using vibrational and quantum chemical calculations

Kamuran SARAÇ[a,*] (iD)

[a] Bitlis Eren University, Faculty of Art and Sciences, Department of Chemistry, TR-13000, Bitlis, Turkey

ABSTRACT

The aim of the study was to synthesize 4-Coumarinyl-4-nitrobenzoate and detect its experimental and theoretical properties. 4-Coumarinyl-4-nitrobenzoate was synthesized using by the nucleophilic adduction-separation reaction of aroyl compounds. In this context 4-coumarinyl 4-nitrobenzoate compound has been characterized both experimentally and theoretically by using quantum chemical calculations and spectral techniques. Quantum chemical calculations such as the molecular geometry, geometric structure, and geometric parameters of the title compound were calculated with the 6-311G (d, p) basis set. Quantum chemical calculations of electronic properties such as energy difference between HOMO-LUMO, chemical hardness and chemical softness were made. Molecular electrostatic potential (MEP) surface of 4-Coumarinyl-4-nitrobenzoate was obtained.

1. Introduction

Coumarins are oxygen-containing heterocyclic compounds isolated from plants, particularly green plants. It is known that there are about 1300 naturally derived coumarin derivatives. It occurs naturally in the fruits, bark, stems and leaves of many plants, including tonka beans, acacia, lavender, apricots, strawberries and cinnamon. In addition to natural coumarins isolated from plants, synthetic coumarin derivatives are also available. Coumarin and its derivatives are used in the treatment of different diseases and exhibit many biological properties such as anticoagulant, antiallergic, antibiotic, diuretic, anti-HIV, antibacterial. It is known that dicumaril and its derivatives, which are among the bisumarins, have anticoagulant effects and these compounds have a reducing effect on blood clotting and are used in the production of therapeutic drugs. Warfarin, which has 4-hydroxycoumarin structure, is the best known anticoagulant. Novabiosin and Chlorobiocin are coumarin derivatives with antibiotic and antibacterial properties and have poor farmo kinetic and toxic

preventive properties [1]. Benzocumarins and benzochromones are compounds that have been studied recently due to their chiocological properties. These compounds are also used in the textile industry as a shine enhancer of synthetic fibers [2]. The photophysical properties of coumarin derivatives differ according to the groups connected in the structure and the solvent medium. Coumarin derivatives find a wide field of study as they have excellent responsiveness for important laser dyestuffs, non-linear optical chromophore and solubility dynamics studies in homogeneous solutions [3]. A significant number of coumarin dyes are used as blue, green and red additives in organic light emitting diodes (OLEDs). However, coumarin dyes easily self-absorb at high concentrations due to intermolecular interactions. Therefore, it should always be used in appropriate concentrations to manufacture OLEDs with luminescent efficiency in light emitting materials [4]. Because of the use of coumarin derivatives in such a wide and diverse field, 4-Coumarinyl-4-nitro benzoate compound was synthesized for the first time in this study with the aim of using it in at least one of these fields. On the other hand, the 4-

Coumarinyl-4-nitrobenzoate compound has been characterized both experimentally and theoretically by using quantum chemical calculations and different spectral techniques. The data obtained from the theoretical calculations were used to calculate the global reactive descriptor and thermodynamic parameters.

2. Materials and Methods

2.1. Experimental

Synthesis and physical properties

To 4-hydroxycoumarin (1.62 g, 10 mmol) in dry pyridine (2 mL, 25 mmol) containing piperidine (1drop) at 0º was slowly added 1.5 equivalent of 4-nitro benzoyl chloride. The reaction mixture was poured into ice and dilute hydrochloric acid. The precipitate was filtered and washed with water. After shaking the product with 5% sodium bicarbonate solution, it was again filtered, washed and recrystallized with ethanol.
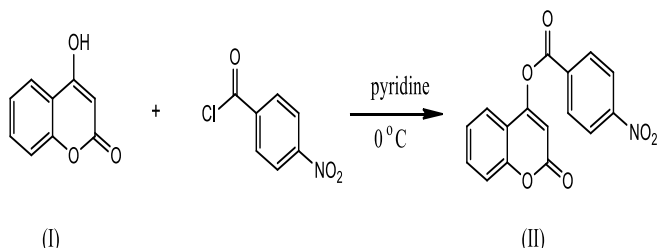

Figure 1. The reaction for the synthesis of title compound [5].

2.2. Computational methods

Gas-phase geometrical optimizations of title compound was performed by using the ab initio method. The relative energy for the two tautomers has been calculated by DFT method at the B3LYP/6-311G(d,p) level of theory [6].
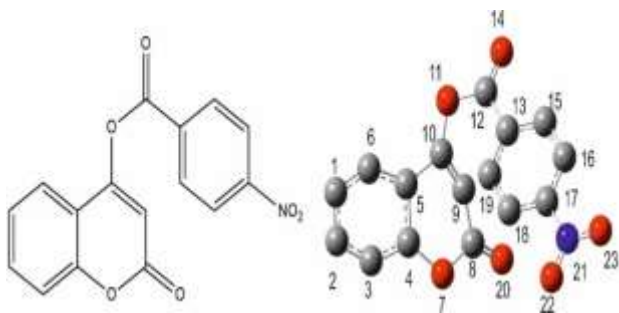

Figure 2. (a) Molecular structure of 4-Coumarinyl-4-nitrobenzoate (b) The theoretical geometric structure of the title compound (with B3LYP/6-311G(d,p) level).

3. Results and Discussion

3.1. Atomics charge distributions in gas-phase and in solutionphase

Atomic charge distributions in gas and solution phases The electronic charge distribution in a molecule as well as the nature of the molecular orbitals (i.e. antibonding, bonding or nonbonding) for certain atom pairs can be characterized using the technique of Mulliken charge distribution [7]. The formation of pairs of donors and acceptors including the charge transfer in the molecule is indicated by the charge distribution over the atoms. Table 1. shows the Mulliken atomic charges for carbon, nitrogen and oxygen atoms of 4-Coumarinyl-4-nitrobenzoate determined at the B3LYP/6-311G(d,p) level with the molecule in gas phase. Additionally, Table 1. also shows the obtained values of the three solvents (chloroform, water and ethanol) which were chosen to determine the solvent effect on the atomic charge distributions of 4-Coumarinyl-4-nitrobenzoate on the basis of the B3LYP/6-311G(d,p) model. According to the Mulliken technique, the negative atomic charges of the O20 atom of pyrone ring, O22 and O23 atoms of benzoate are larger compared to the gas phase. On the other hand, the O20, O22 and O23 atoms have not show any significant change in atomic charge values between gas phase and solution phases.

3.2. Nuclear magnetic resonance (NMR) spectra and Vibrational assignments

The Hydrogen in the 1H NMR spectrum of the coumarin was observed as singlet at 7,10 ppm. The protons (8H) coumarin and benzoyl were observed as a multiplet in the range of 7.50-8.20 ppm. Chemical shift of all carbons in coumarin and benzoyl ring were shown between 115 and 138 ppm. The C-O stretching vibration in Coumarin was observed in the 1250-850 cm-1 region [8]. In the present study, the C-O streching vibration was observed at 1172 cm-1. The C=O stretching frequency was observed in the range of 1600-1850 cm-1 owing to its large change in dipolemoment and its characteristic frequency used to study a wide range of the compounds [9]. The C=O stretching vibration in title compound was observed at 1733 cm-1. All these data confirm the structure of the compound.

Table.1. Atomic charges (e) of the title compound in gas phase and solution phase.

Atom	Gas	Chloroform	Ethanol	Water
C1	-0.334171	-0.334170	-0.334170	0.334170
C2	-0.252517	-0.252518	-0.252518	-0.252518
C3	-0.406281	-0.406281	-0.406281	-0.406281
C4	0.545140	0.545140	0.545140	0.545140
C5	0.128568	0.128569	0.128569	0.128569
C6	-0.321010	-0.321010	-0.321010	-0.321010
O7	-0.534787	-0.534787	-0.534787	-0.534787
C8	1.157896	1.157896	1.157896	1.157896
C9	-0.649202	-0.649201	-0.649201	-0.649201
C10	0.536222	0.536221	0.536221	0.536221
O11	-0.488570	-0.488570	-0.488570	-0.488570
C12	0.921118	0.921118	0.921118	0.921118
C13	0.061170	0.061170	0.061170	0.061170
O14	-0.826672	-0.826672	-0.826672	-0.826672
C15	-0.271796	-0.271796	-0.271796	-0.271796
C16	-0.258750	-0.258749	-0.258749	-0.258749
C17	0.496510	0.496510	0.496510	0.496510
C18	-0.306465	-0.306464	-0.306464	-0.306464
C19	-0.363628	-0.363629	-0.363629	-0.363629
O20	-0.826024	-0.826025	-0.826025	-0.826025
N21	0.811344	0.811344	0.811344	0.811344
O22	-0.617032	-0.617031	-0.617031	-0.617031
O23	-0.618195	-0.618195	-0.618195	-0.618195

3.3. The frontier molecular orbitals

Frontier Molecular orbitals (FMO's) generally play an essential role in chemical reactions, UV-vis spectra, optical and electrical properties. Also recently, the energy gap (ΔE) of HOMO-LUMO has been used to prove the chemical activity and the bioactivity from intra molecular charge transfer [10]. The 3D plots of the HOMO-1,HOMO,LUMO,LUMO+1 orbitals were calculated at the B3LYP/6-311G (d,p) and shown in Figure 3. As seen from the Figure 3, the LUMO is located on nitro group and benzene ring, the HOMO is more located on the coumarin ring and partially over the carbonyl group.

The ability of electron accepting and giving defines for LUMO and HOMO, respectively. Besides, the HOMO-LUMO energies and their energy gap (ΔE) are calculated with the B3LYP/6-311G(d,p) method. The global chemical reactivity and density functional descriptors of the title compound such as dipole moment (μ), electron affinity (A), electronegativity (χ), chemical potential (μo), ionization potential (I), global hardness (η), electrophilicity index (ω) and global softness (ζ) are calculated from the energies of the HOMO and the LUMO at B3LYP/6-311G (d,p) basis set and are given in Table 2.
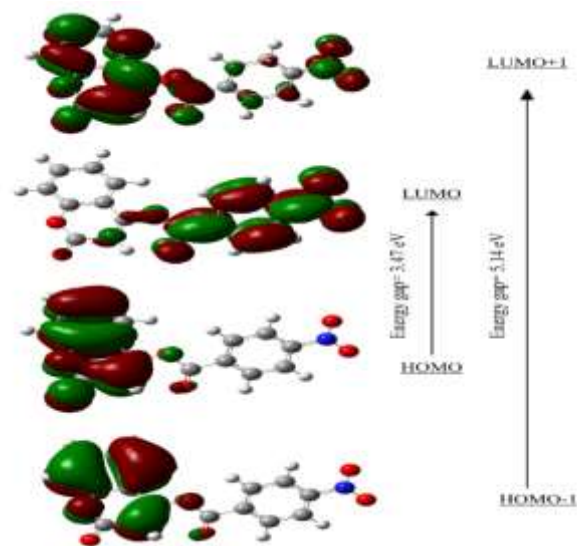

Figure 3. Molecular orbital surfaces and energy levels given in parentheses for the HOMO, HOMO-1, LUMO and LUMO-1 of the title compound computed at B3LYP/6-311G(d,p) level.

Table 2. Electronic structure parameters of the title compound.

Parameters	B3LYP 6-31G(d,p)
E_{LUMO} (eV)	-3.2264
E_{HOMO} (eV)	-6.6969
$\Delta E = E_{LUMO} - E_{HOMO}$ (eV)	3.4705
A (eV)	3.2264
I (eV)	6.6969
ζ (eV)	0.5763
μ_o (eV)	-4.9616
η (eV)	1.7352
ω (eV)	7.0935
χ (eV)	4.9616

These parameters can be calculated as follows [11].

When the chemical hardness is considered, a molecule having a small HOMO–LUMO energy gap means a soft molecule and large energy gap means a hard molecule. It may also relate to the stability of the molecule against hardness. That is, the molecule with least energy gap is less stable and more reactive. The calculated values of ζ, ⬚, EHOMO ELUMO, ΔE, μo and ⬚ for the title compound are 0.57, 1.73, 6.69, 3.22, 3.47, -4.96 and 4.96 eV, respectively. Taking into account the value of the energy between HOMO and LUMO, it is shown that charge transfer is within the title compound. Besides, as shown in Table 2, the chemical potential is negative and it means that the title compound is stable.

3.4. Molecular electrostatic potential (MEP)

Molecular electrostatic potential (MEP) is related to the electron density and serves a very useful descriptor to explain nucleophilic and electrophilic reaction regions, hydrogen bonding interactions, structure-activity relationship of molecules containing drugs and biomolecules [12]. Molecular electrostatic potential surfaces were mapped by using B3LYP/6–311G (d,p) basis set to predict reactive sites of electrophilic and nucleophilic attacks for the title compound as shown in Figure 4.

The different values of the electrostatic potential are shown by different colors at the surface; namely, blue, green and red colors show the regions of the most positive electrostatic potential, zero potential, the regions of the most negative electrostatic potential, respectively [13].

Potential decreases in the order blue > green > yellow > orange > red. The positive regions related to nucleophilic reactivity (blue color), whereas the negative regions of MEP related to electrophilic reactivity (red and yellow colors). As seen in Figure 4, From the molecular, it is evident that the negative regions are mainly localize over the carbonyl group rather than oxygen atoms, the positive regions are mostly localized over hydrogen atoms.

Consequently, it is expected that the more electronegativity in the carbonyl group makes it the most reactive sites for electrophilic attack, whereas the hydrogen atoms are the most reactive for nucleophilic attack in title compound.

4. Conclusions

Electronic investigations of 4-Coumarinyl-4-nitro benzoate has been carried out were calculated using the B3LYP method using 6-311G (d,p) basis set show the molecular geometry parameters. By mapping an electrondensity isosurface with molecular electrostatic potential surface, information about the shape, size, and site of high electronegativity and charge distribution of the title compound has been obtained. Using the B3LYP/6-311G(d,p) method, which provide, the energies of HOMO&LUMO and their orbital energy gaps were calculated as well as the physical and structural properties of the molecules. 3.47 eV was found to be the frontier orbital energy gap (EHOMO-ELUMO). With the aid of the theoretical calculations at the B3LYP/6-311G(d,p) level. The positive potential sites are around the hydrogen atoms and the negative potential sites are on electronegative atoms, which are shown by the MEP map. The region from where the compound may have intermolecular interactions can be understood based on this information provided.

References

[1] Bouasla, S., Amaro-Gahete J., Esquivel, D., López, M.I., Jiménez-Sanchidrián, C., Teguiche, M., Romero-Salguero, F. 2017. Coumarin derivatives solvent-free synthesis under microwave irradiation over heterogeneous solid catalysts. Molecules, 22 (12), 2072-2080.

[2] Kolancılar, H. 2019. DFT Yöntemi Kullanılarak 1,3-Bis-{(2-Aminobenzoil) Amino} Propanın Teorik Hesaplamaları ve Bu Değerlerin Literatürdeki Deneysel Değerler ile Karşılaştırılması. Düzce Üniversitesi Bilim ve Teknoloji Dergisi, 7 (3), 1319-1334.

[3] Abdel, M.S.A., Hamed E., Saif, M., Hafez S. 2018. Binding, and thermodynamics of βcyclodextrin inclusion complexes with some coumarin laser dyes and coumarin-based enzyme substrates: a simulation study. Journal of Inclusion Phenomena and Macrocyclic Chemistry, 92 (3), 319-327.

[4] Yu, T., Zhu, Z., Bao Y., Zhao, Y., Liu, X., Zhang, H. 2017. Investigation of novel carbazolefunctionalized coumarin derivatives as organic luminescent materials. Dyes and Pigments, 147 (1), 260-269.

[5] Babinski, D., Soltani, O., Frantz, D.E. 2008. Stereoselective synthesis of acetoacetate-derived enol triflates. Organic Letters, 10 (13), 2901-2904.

[6] Vignale, G., Rasolt, M., 1987. Density-functional theory in strong magnetic fields. Phys. Rev. Lett. 59, 2360–2363.

[7] Arunagiri, C., Arivazhagan, M., Subashini, A., Maruthaiveeran, N. 2014. Theoretical and experimental calculations, Mulliken charges and thermodynamic properties of 4-chloro-2-nitroanisole. Spectrochim. Acta Part A Mol.Biomol. Spectrosc, 131, 647-656.

[8] Karakas, S,E., Dereli, Ö. 2013. Molecular structure and vibrational spectra of 7-Methoxy-4-methylcoumarin by density functional method. J Mol Struct.1052, 214-20.

[9] Lin-Vien, D., Fateley, WG., Grasselli, J.G., Colthup, N.B.,1991. The Handbook of Infrared and Raman Characteristic Frequencies of Organic Molecules, Academic Press.

[10] Fleming, J., 1976. Frontier Orbitals and Organic Chemical Reactions, John Wiley, London.

[11] Lee, C., Yang, W., Parr, R.G., 1988. Local softness and chemical reactivity in the molecules CO, SCN– and H2CO. Journal of Molecular Structure: Theochem, 163, 305-313.

[12] Luque, F.J., López, J.M., Orozco, M., 2000. Perspective on Electrostatic interactions of a solute with a continuum. A direct utilization of ab initio molecular potentials for the prevision of solvent effects. Theoretical Chemistry Accounts, 103, 343-345.

[13] Sebastian. S., Sundaraganesan. N., 2010. The spectroscopic (FT-IR, FT-IR gas phase, FT-Raman and UV) and NBO analysis of 4-Hydroxypiperidine by density functional method. Spectrochimica Acta Part A: Molecular and Biomolecular Spectroscopy, 75 (3), 941-952.
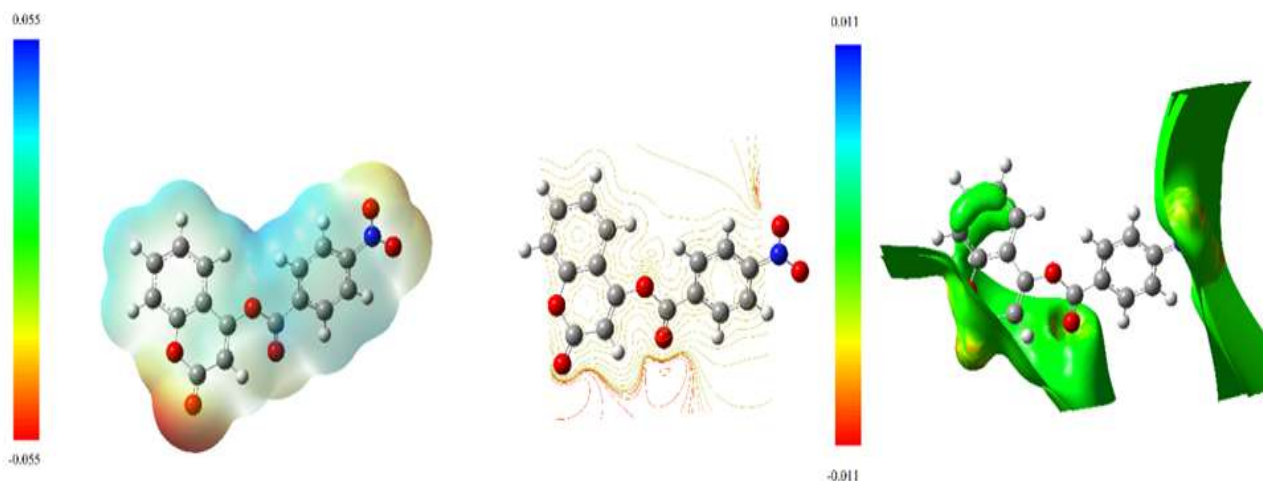
Figure 4. Molecular electrostatic potential maps of the title compound